energies

MDPI

Article

Thermal Performance of a Novel Non-Tubular Absorber with Extended Internal Surfaces for Concentrated Solar Power Receivers

Xinchen Na, Yingxue Yao * and Jianjun Du

School of Mechanical Engineering and Automation, Harbin Institute of Technology (Shenzhen), HIT Campus of University Town of Shenzhen, Shenzhen 518055, China; naxinchen@stu.hit.edu.cn (X.N.); jjdu@hit.edu.cn (J.D.)
* Correspondence: yyx@hit.edu.cn; Tel.: +86-0755-26036868

Abstract: A non-tubular prototype cavity receiver absorber with extended internal surfaces (fins) is proposed to enhance heat transfer in Stirling engine-based Concentrated Solar Power systems. There is limited research on the realization of downsized absorbers in terms of their design and manufacturing. The objective of the absorber solution proposed in this paper is to address the issue of inadequate comprehension regarding the impacts of the geometric and flow parameters on thermohydraulic efficiency. These impacts are numerically investigated in a 100 mm long heat transfer channel with a 10 mm × 10 mm section. The prototype absorber is fabricated using a wire electrode-discharging manufacturing approach, and is experimentally investigated using the enthalpy method. Numerical results indicate that heat transfer to the working fluid in the novel absorber can reach 482 W at the reasonable cost of 0.391% pressure drop per 100 mm (air flow at 0.0015 kg/s and 5 bar). In the experimental investigation, the prototype realizes a 1113.033 W heat transfer rate at 8 bar and 12 kg/h. This implies that a non-tubular design with extended internal surfaces can increase the internal surface area to enhance heat transfer while downsizing the volume to reduce heat loss.

Keywords: solar receiver absorber; extended surfaces; heat transfer enhancement; numerical and experimental investigations

check for updates

Citation: Na, X.; Yao, Y.; Du, J. Thermal Performance of a Novel Non-Tubular Absorber with Extended Internal Surfaces for Concentrated Solar Power Receivers. *Energies* **2023**, *16*, 5055. https://doi.org/10.3390/en16135055

Academic Editor: Jesús Polo

Received: 15 May 2023
Revised: 5 June 2023
Accepted: 27 June 2023
Published: 29 June 2023

Copyright: © 2023 by the authors. Licensee MDPI, Basel, Switzerland. This article is an open access article distributed under the terms and conditions of the Creative Commons Attribution (CC BY) license (https://creativecommons.org/licenses/by/4.0/).

1. Introduction

Concentrated solar power (CSP) presents a promising means of utilizing renewable energy due to its high conversion efficiency and potential to overcome the inherent limitations of renewable energy sources in terms of discontinuity and dispersibility. This may help in overcoming the climate change and energy shortage crises as well as in achieving sustainable development goals [1]. In a typical CSP system, solar radiation is concentrated onto the cavity receiver, specifically, the absorber in the receiver, where it is converted into thermal energy in the working fluid. The absorber is a critical heat-exchanging component that directly impacts the system's conversion efficiency and cost [2]. To improve passive heat transfer in a heat exchanger, one effective approach is the implementation of extended surfaces [3].

An (internally) finned tube is a common form used to apply the idea of extended surfaces to enhance heat transfer; however, the application of such tubes is limited by the trade-off between increased heat transfer and increased pressure drop. Nada et al. [4] used computational fluid dynamics (CFD) to investigate natural convection air flow and heat transfer in unfinned tubes and tubes with finned-horizontal annulus. They found that heat transfer increases with the annulus thickness, convection, number of fins, and fin width. Ammar Ali et al. [5] computationally analyzed the pressure drop and heat transfer characteristics of smooth tubes and internal helical micro-finned tubes with two different heights. They discovered that thermal performance was enhanced by fins at the expense of

increased pressure drop. Lin et al. [6] experimentally compared single-phase and two-phase heat transfer and pressure drop in five types of micro-fin tubes. Their results suggested that micro-fin tubes could drastically increase heat transfer coefficients. Wei et al. [7] developed a comprehensive performance model of heat transfer tubes and experimentally evaluated previous correlations. They found that the heat transfer coefficient and pressure drop both increase with the mass flux and condensation temperature. Tang et al. [8] numerically investigated the impact of fin shape and helical angle on the heat transfer coefficients during refrigerant condensation. They found a positive correlation between the heat transfer coefficients and both the mass velocities and vapor quality. Zhang et al. [9] studied the effects of fin geometric parameters on the thermohydraulic performance of air cross-flow in the tubes. Their results showed that fin height had a significant effect on heat transfer and flow resistance in three-dimensional finned tubes. Tang et al. and Zhang et al. developed empirical correlations for the heat transfer enhancement ratio and pressure drop deterioration, respectively. This limitation becomes more noticeable in downsized applications where the tubular structure is constrained by size. Therefore, exploring alternative designs that can reduce heat resistance without increasing pressure drop or compromising mechanical strength is necessary.

Most researchers use water or refrigerant as the working fluid in heat exchangers. Pressurized air, however, is relatively easier to generate compared to other types of working fluids, and does not require additional transportation or strict sealing. This has led to expansion of the scope of application of pressurized air systems. Duan et al. [10] investigated turbulent flow and heat transfer characteristics of different fin geometries, finding that a blossom-shaped fin outperformed a wave-like fin when pressure drop was strictly restricted. Kim et al. [11] experimentally investigated the pressure drop and heat transfer characteristics of a wavy-finned recuperator and found that an increase in the fluid mean specific volume due to temperature increase resulted in a larger pressure drop and insignificant variation in effectiveness. Lotfi et al. [12] computationally analyzed the heat transfer and pressure drop characteristics of the flow in smooth wavy-finned and elliptical tube heat exchangers, finding that vortex generators could bring about further heat transfer enhancement by adjusting the position, type, and attack angle of vortex generators. Despite the potential advantages of pressurized air systems, it is important to note that air has a relatively low heat transfer capability, which may limit its feasibility in downsized systems.

Heat sinks are commonly used as cooling devices and air conditioning systems [13,14], and researchers have dedicated much effort to investigating their thermal performance. Dastmalchi et al. [15] studied heat transfer and pressure drop changes in a heat sink, and found that increasing the micro-fin height and decreasing the helix angle improved heat transfer in turbulent flows. Freegah et al. [16] proposed a new thermal design of plate-fin heat sinks attached to half-round pins, which showed superior thermal performance in comparison with corrugated or symmetrical half-round hollow pins. Hussain et al. [17] investigated the effect of flow direction on the thermal performance of plate-fin heat sinks with fillet profiles, and found that the proposed heat sink had reduced base temperature and thermal resistance. Sahel et al. [18] numerically examined the hydrothermal performance of a heat sink with hemispherical pin fins, finding that it outperformed a heat sink with staggered cylindrical pin fins. Yan et al. [19] proposed a novel fin-shaped pin–fin array heat sink to enhance microfluidic cooling in electronic chips. A staggered micro-fin-shaped A pin–fin demonstrated superior hydrothermal performance by affecting the flow separation point and vortex size. Singh et al. [20] explored the heat transfer characteristics of embossed heat sinks subjected to natural convection and found that the Nusselt number for embossed fin increased with the impression angle and pitch. The effect of heat sink geometries on the performance of a thermoelectric generator was researched by Özbektas et al. [21], who found that the electrical output increased with increasing air velocity and surface temperature. The application of heat sinks with a similar structure in a heat exchanger devices has not been thoroughly investigated, nor have the pressurized directional flow characteristics or the impact of the geometric parameters.

Our research proposes a non-tubular pressurized absorber for CSP receivers that utilizes extended surfaces (macro-fins) to enhance heat transfer. Previous studies of the thermal performance of micro-fins or macro-fins in cooling [22] or heat exchange [23] systems have provided theoretical support for the proposal in this article. The feasibility of reshaping the absorber to a flat geometry has been verified in previous research [24]. To apply such a novel design in the context of CSP systems, the following issues are addressed in this paper:

- The non-tubular alternative design needs to balance heat transfer enhancement, pressure drop, and downsized geometry. The feasibility of fabricating the extended surface in the absorber must be considered. Meanwhile, careful design is required to ensure that the removal of the tubular structure does not negatively impact the structural integrity of the system.
- Further research is needed to explore the feasibility and potential of pressurized air in downsized applications and identify strategies to overcome the limitations associated with the low heat transfer capability of air.
- The proposed structure is inspired by the design of a heat sink. Instead of ambient air, which transfers heat through passive convection, in our case the working fluid is pressurized directional air flow. Thus, the parameters that affect the heat transfer in heat sinks must be re-evaluated. This research gap highlights the need for further exploration and analysis in this area.

The proposed design idea for downsizing the absorber and fabricating the fins into its internal surfaces has not been previously researched. Thus, a comprehensive numerical and experimental investigation is performed to compare the heat transfer of airflows with various parameters in channels of different geometric parameters in order to provide information for verifying, analyzing, and optimizing this type of pressurized air receiver.

2. Numerical Modeling of the Novel Absorber

2.1. Design Description

The proposed novel non-tubular absorber design to reduce heat loss and enhance heat transfer is briefly demonstrated in Figure 1.

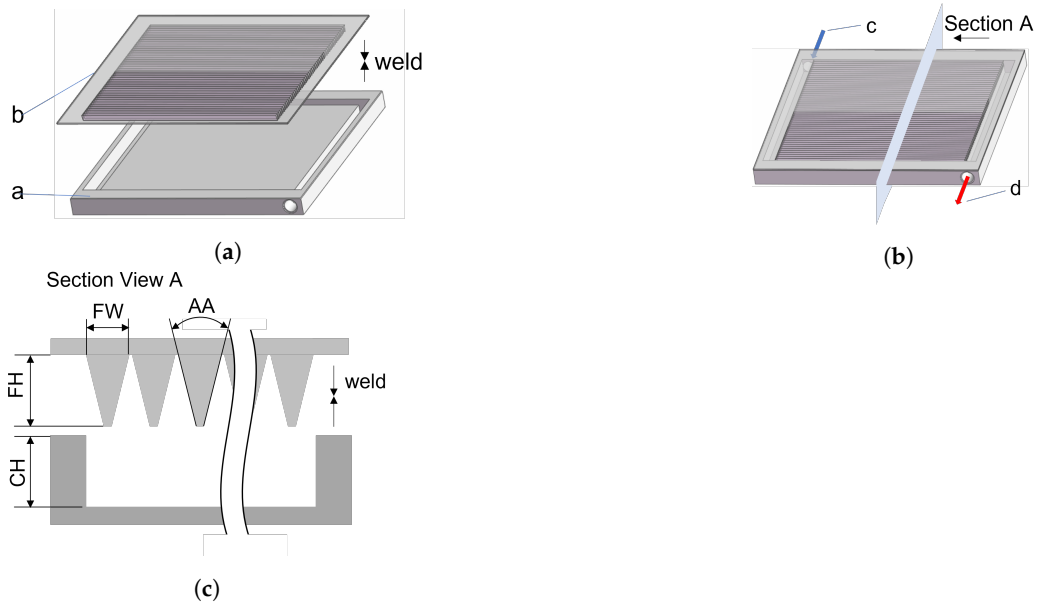


Figure 1. Structural scheme of the novel absorber: (**a**) parts before welding; (**b**) welded absorber; and (**c**): section view. Components and working fluid: a, bottom plate; b, heat transfer plate with extended surfaces; c, incoming cold air; d, hot air. Dimensions in section view: CH, channel height; FH, fin height; FW, fin width; AA, fin apex angle.

As shown in Figure 1, the non-tubular configuration features a planar external geometry and comprises two distinct components, namely, the heat transfer plate and the bottom plate (b and a in Figure 1). The fins are fabricated into the internal surface of the heat transfer plate through either WEDM or milling techniques. Upon welding the two components, the fins form channels that facilitate the flow of pressurized air, which undergoes heating in the interval spaces between the fins. The non-tubular configuration is capable of withstanding high pressure, with the fins serving as effective stiffeners.

The geometric parameters of the fins impact the thermal resistance R_t, which is derived from *Fourier's law of heat conduction* for the wall, commonly expressed as

$$R_t = L/(kA_h) \quad (1)$$

In this case, k is the thermal conductivity of steel, which is constant when compared at an equal temperature, L is the nominal thickness of the heat transfer plate in Figure 1, and A_h is the heat transfer area. For the design in Figure 1, all heat transfer plates are made of steel containing parallel channels with isosceles triangle sections formed by the fabricated fins. Here, we set a channel height of 5 mm and limit the fins within a 160 mm × 160 mm projected area; reasonable intervals between the fins and at the apex are included as well. The approximate ratios of L/A_h in the new design are listed in Table 1 for different fin heights of 5 mm, 3.75 mm, and 2.5 mm and apex angles of 15 °C and 30 °C.

For identical units of channel volume or external volume, a larger heat transfer area leads to better heat transfer or reduced heat loss. These ratios are calculated and presented in Table 1.

Table 1. Geometric ratios for dimensional parameters.

	Fin Height (mm)	Fin Width (+Internal, mm)	L/A_h (mm/mm^2)	A_h/Int.V. * (mm^2/mm^3)	A_h/Ext.V. ** (mm^2/mm^3)
Apex angle 15 °C	5	1.8 (+0.2)	2.80×10^{-5}	2.51	1.81
	3.75	1.35 (+0.15)	2.28×10^{-5}	1.87	
	2.5	0.9 (+0.1)	1.76×10^{-5}	1.51	
Apex angle 30 °C	5	3 (+0.2)	4.13×10^{-5}	1.41	1.14
	3.75	2.25 (+0.25)	3.39×10^{-5}	1.05	
	2.5	1.5 (+0.1)	2.64×10^{-5}	0.92	
No fins	–	–	3.91×10^{-5}	0.2	0.34
Tubes	–	1.5 + 0.75 ***	1.78×10^{-5}	0.92	1.14

* Internal channel volume; ** external volume of the absorber; *** internal radius + wall thickness.

The width of the fin is determined by its height and apex angle. In this research, the manufacturers were able to successfully fabricate fins with a width of 1.8 mm through WEDM techniques. However, in order to mitigate deformation resulting from heat generated during wire cutting machining, it is recommended that the fin width exceed 2 mm for mass production. In general, minimal apex angle and fin width subject to manufacturing is preferable. In the design of this study, apex angles smaller than 15 °C are not applicable.

The maximum fin height must not surpass the channel height. It can be deduced from Table 1 that a greater fin height may result in a higher thermal resistance. On the contrary, it should be noted that in such a case the heat transfer area within a given volume is significantly increased. Therefore, determining which factor should prevail requires further investigation.

2.2. Numerical Model

With the introduction of the extended surface, comprehensive CFD modeling of the entire structure would result in an excessive number of elements. The finite element method (FEM) calculation would be impractical due to the high computational demands and time

consumption. Instead, based on prior literature research on the heat transfer mechanisms of cooling devices featuring multi-scale structures [25], a simplified model is employed to evaluate the heat transfer from the absorber's internal extended surfaces to the working fluid using the CFD method in ANSYS Fluent.

The computational domain is a rectangular prism. As shown in Figure 2, the section is a square of 10 mm × 10 mm and the domain length is 100 mm. The solid bodies in the model are all made of steel. The fluid is an ideal gas which enters the domain from one section (as the mass flow inlet) and leaves from another section (as the pressure outlet).

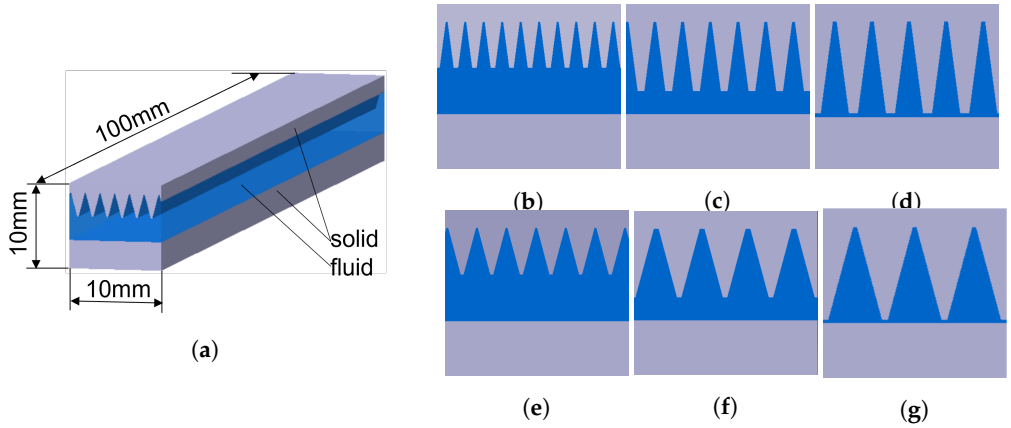


Figure 2. Numerical model: (**a**) the calculation domain, with different sections parameters: apex angel 15° with a fin height of (**b**) 2.5 mm, (**c**) 3.75 mm, and (**d**) 5 mm * and apex angel 30° with a fin height of (**e**) 2.5 mm, (**f**) 3.75 mm, and (**g**) 5 mm *. The * means that a 0.2 mm interval exists between the fin and the bottom plate.

3. Numerical Method

3.1. Governing Equations

Heat transfer in the three-dimensional model is simulated using the CFD software FLUENT. The working fluid between the solid parts is a steady state ideal gas (air). All solid parts are made of uniform steel material. A final realizable k-ε turbulence model with standard wall functions which generates identical heat flux (of 0.4% error) to the results of a laminar model in separate calculations is employed. The governing equations for continuity, momentum, and energy are adapted in the computational domain according to the *ANSYS Fluent Theory Guide 2022*, and the citation for these equations is listed in Appendix A.

3.2. Boundary Conditions and Numerical Methods

The definitions of the boundaries are illustrated in Figure 3. The mass flow inlet boundary condition is established for the incoming fluid, for which a constant mass flow rate, pressure, and temperature are maintained. The pressure outlet boundary condition is applied to the fluid outlet. A stationary wall boundary condition with a non-slip shear condition is utilized on all wall boundaries within the domain. The high and low plains of the solid are set to a static temperature. The external surfaces on the side are subjected to an adiabatic wall boundary condition with a heat flux of 0.

Fluid–solid coupled heat transfer between the fin surfaces and fluid was modeled for both heat conduction and convection. A coupled algorithm scheme was adopted to deal with the coupling of pressure and velocity. Second-order upwind methods were applied for the spatial discretization of momentum, turbulence, and energy. The convergence criterion was taken as 1×10^{-3} for the flow equations and 1×10^{-6} for the energy equation.

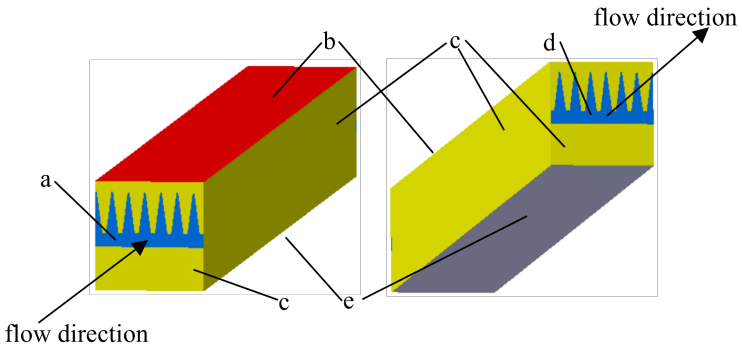


Figure 3. Boundary conditions: a, mass flow inlet; b, wall (high temperature); c, wall (adiabatic, heat flux = 0); d, pressure outlet; e, wall (low temperature).

3.3. Grid Generation

Non-uniform grids were applied to the computational domain. Figure 4 shows the enlarged mesh structure in the mass flow inlet plain of the computational domain fin height = 3.75 mm. As shown in Figure 4, an unstructured mesh was applied in all zones (solid and fluid). The fluid part and high-temperature solid part were meshed using tetrahedron elements to acquire finer heat transfer results between the solid and fluid. The solid part with lower temperature was meshed automatically using tetrahedron elements on the solid–fluid boundary and hexahedron elements internally.

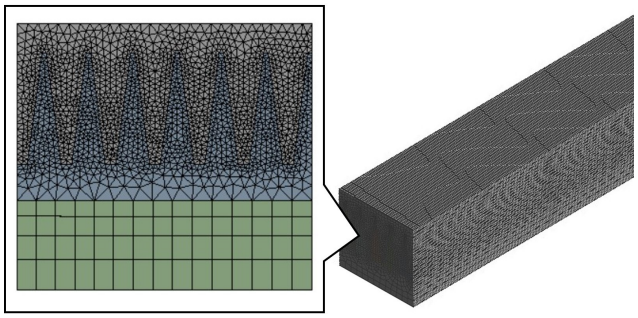


Figure 4. Meshing of the computational domain.

To ensure that the CFD solution was independent of the grid size, we compared models meshed with respective element sizes of 1 mm and 1.5 mm and respective minimum element sizes of 0.05 mm, 0.1 mm, and 0.2 mm at the solid–fluid boundary. This comparison found that the relative errors of heat transfer rates in these setups were negligible. Consequently, an element size of 1.5 mm with a minimum size of 0.2 mm was selected to reduce the calculation time.

3.4. Additional Numerical Analysis

3.4.1. Additional CFD Analysis

CFD analyses in the 10 mm × 10 mm × 100 mm domain cannot sufficiently investigate the fluid characteristics and temperature distribution in the channel. Thus, two additional numerical analyses employing slightly modified numerical models were used to investigate the flow characteristics and temperature distribution within the channel. The detailed CFD analyses are illustrated in Appendix B.

3.4.2. Static Structural Analysis

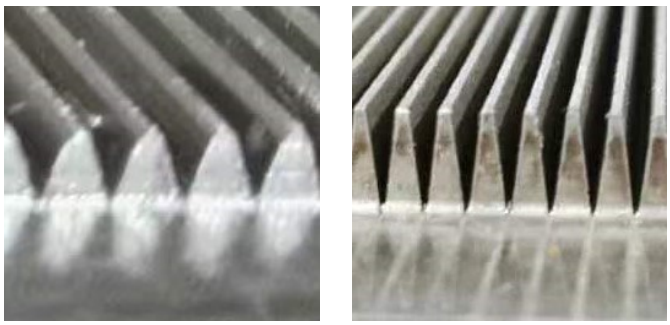
The heat transfer plate's strength and stiffness are critical parameters to the feasibility of the novel absorber. According to literature, the working pressure in Stirling systems is generally lower than 3 MPa; thus, a maximum pressure of 1.5 MPa is adapted in this research. However, certain Stirling engines do work under pressures as high as 10 MPa.

Thus, a maximum pressure of 10 MPa was applied in the static structural analysis to determine whether the safety margin was sufficient. The detailed FEM static structural analysis is illustrated in Appendix C.

4. Experimental Investigations

4.1. The Novel Absorber with Extended Internal Surfaces

The fins located in the internal channels can be fabricated using either milling or WEDM techniques. Milling techniques are suitable for fins with apex angles of 30°, as shown in Figure 5a. On the other hand, fins with an apex angle of 15° should be processed using WEDM technique. WEDM can generate fins with smaller intervals and higher roughness. Though the processing takes longer than traditional milling techniques, WEDM is capable of generating 0.02 mm chamfer diameters. Within the parameter range of this research, WEDM is the preferable machining method. The wire-cut fins are illustrated in Figure 5b.

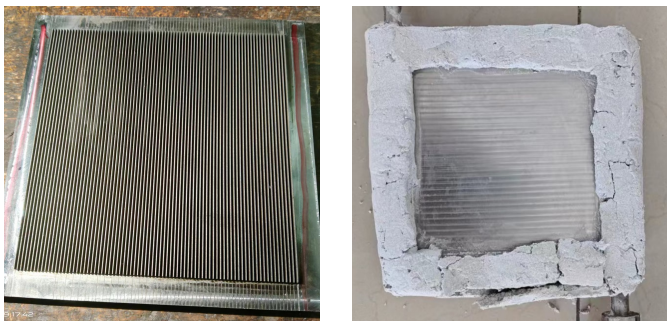


(**a**) (**b**)

Figure 5. Manufactured fins: (**a**) milled fins with a height of 3.75 mm and apex angle of 15° and (**b**) wire-cut fins with a height of 5 mm and apex angle of 30°. Note that only the part shown in (**b**) is used in this paper.

As described in Section 2.1, a 160 mm × 160 mm fin array formed by 80 fins is illustrated in Figure 6a. The fins are 5 mm in fin height with a 15° apex angle. They were processed using WEDM on a stainless steel plate. The remaining metal plate supporting the fins is 20 mm thick, which is sufficient to avoid deformation during the EDM manufacturing and welding processes.

After welding the finned plate with the bottom plate and connectors, material amounting to a thickness of 19 mm was removed. The finished absorber with heat insulation treatment is presented in Figure 6b. The bulk volume of the absorber is 190 mm × 190 mm × 10 mm.



(**a**) (**b**)

Figure 6. Manufactured plate and welded absorber: (**a**) fins processed using WEDM on metal plate and (**b**) welded absorber with insulating paint. Note that additional porous insulation materials were used over the paint.

4.2. Experimental System and Procedures

An experimental simulated system was designed to examine the heat transfer in the novel absorber using the enthalpy method described in Figure 7. The heat transfer to the working fluid can be acquired using the mass flow rate and enthalpy prior to and after passing through the absorber.

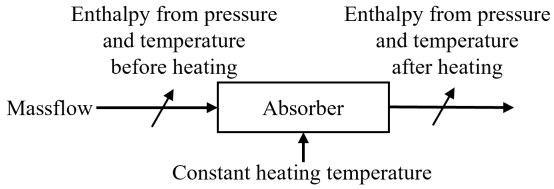


Figure 7. Experimental scheme.

Figure 8 shows the composition of the experimental system. In addition to the prototype absorber, the main system components include an air compressor, a gas booster, a flat panel heater, gauges, and valves.

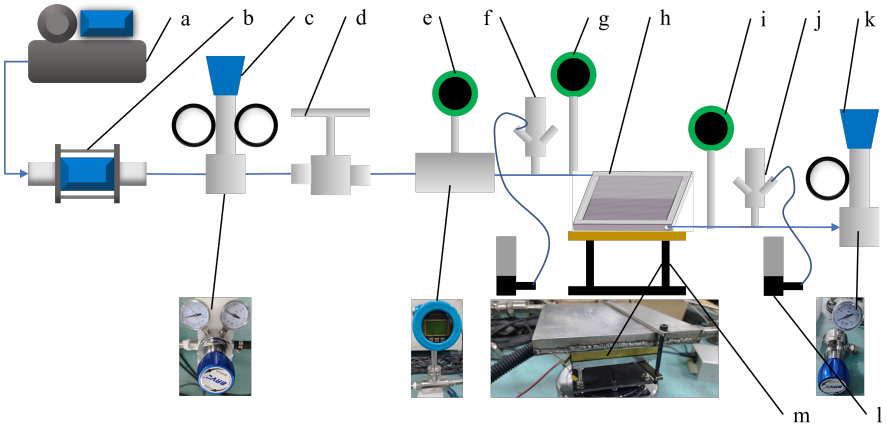


Figure 8. Experimental system: a, air compressor; b, air booster; c, pressure reducing valve; d, throttle valve; e, flow meter; f, thermal couple; g, pressure gauge; h, the proposed absorber; i, pressure gauge; j, thermal couple; k, back pressure valve; l, cooling pump; m, flat panel heater.

During the experimental procedure, the ambient air was compressed to a pressure of 1 MPa (gauge) using a piston air compressor and a gas booster. The air pressure within the receiver was effectively stabilized at 0.8 MPa (gauge) by adjusting the reducing valve and the back pressure valve located upstream and downstream of the receiver, respectively. The flow rate was regulated and measured by a throttle valve and a flow meter, respectively, which were placed immediately after the reducing valve. A 2 kW electric planar heater was utilized to simulate the concentrated solar power. The heater was able to maintain a maximum heating temperature of 873.15 K or 600 °C with an uncertainty of ±2.5 °C.

To measure the inlet pressure and pressure drop across the receiver, pressure transmitters were installed before and after the receiver. Similarly, thermocouples located before and after the receiver were used to measure the inlet temperature and increase in temperature within the receiver. In addition, a flow meter was employed to determine the mass flow rate and enthalpy of the airflow, allowing calculation of the heat transfer within the absorber.

5. Results and Discussion

5.1. Fluid Flow and Temperature

The path lines traced from the inlet to the outlet are depicted in Figure 9a, revealing the generation of the smooth (mainly laminar) flow within the novel WEDM precessed finned channels of the absorber when utilizing turbulent models with laminar zones. Thus,

both laminar and turbulent models are feasible in this research. The fins themselves cause minimal momentum change, with the flow direction changing only upon entry and exit from the finned channels. To minimize the pressure drop and momentum change, it is essential to ensure a sufficient sectional area in the structure before and after the finned channels.

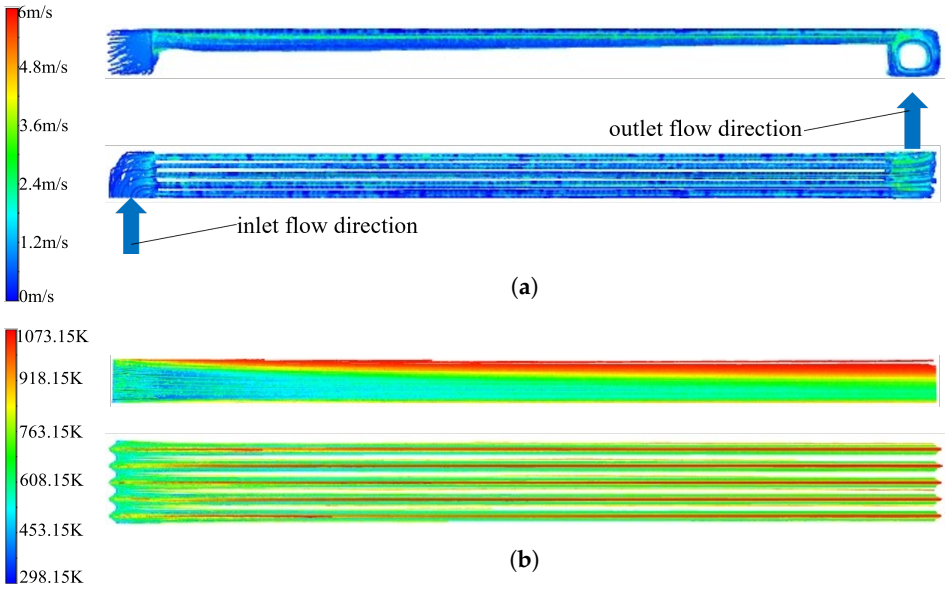


Figure 9. Fluid temperature distribution in the channel: (**a**) flow distribution in the channel and (**b**) temperature distribution in the 160 mm channel. Fluid at the inlet: 0.001 kg/s, 25 °C @10 bar; heat source: constant 800 °C.

Figure 9b displays the temperature distributions of the air flow as it is gradually heated in the designed finned channels. Figure 10 displays the respective temperature distributions in the outlet section vertical to the flow direction and parallel to the inlet section when the initial temperature is 25 °C, 300 °C, 500 °C, and 700 °C in finned channels with an apex angle of 30° and heights of 2.5 mm, 3.75 mm, and 5 mm. The respective outlet temperature distributions in finned channels with an apex angle of 15° are displayed in Figure 11.

The implementation of WEDM-processed fins can effectively reduce the distance between the heat transfer surface and center of the flow. This leads to an improvement in the outlet temperature distribution. As shown in Figures 10 and 11, for an initial temperature of 25 °C the temperature distributions in most examined setups are noticeably non-uniform. Specifically, the air temperature near the flow center is significantly lower than the temperature near the heat transfer surfaces. However, for the cases in which the apex angle is 15° and the fin height is either 3.75 or 5 mm, the outlet temperature is much more uniformly distributed. These results suggest that the temperature distribution improves along the finned channels as the incoming air flow is heated. Consequently, the outlet temperature in all finned channels becomes uniformly distributed even before the initial temperature exceeds 300 °C.

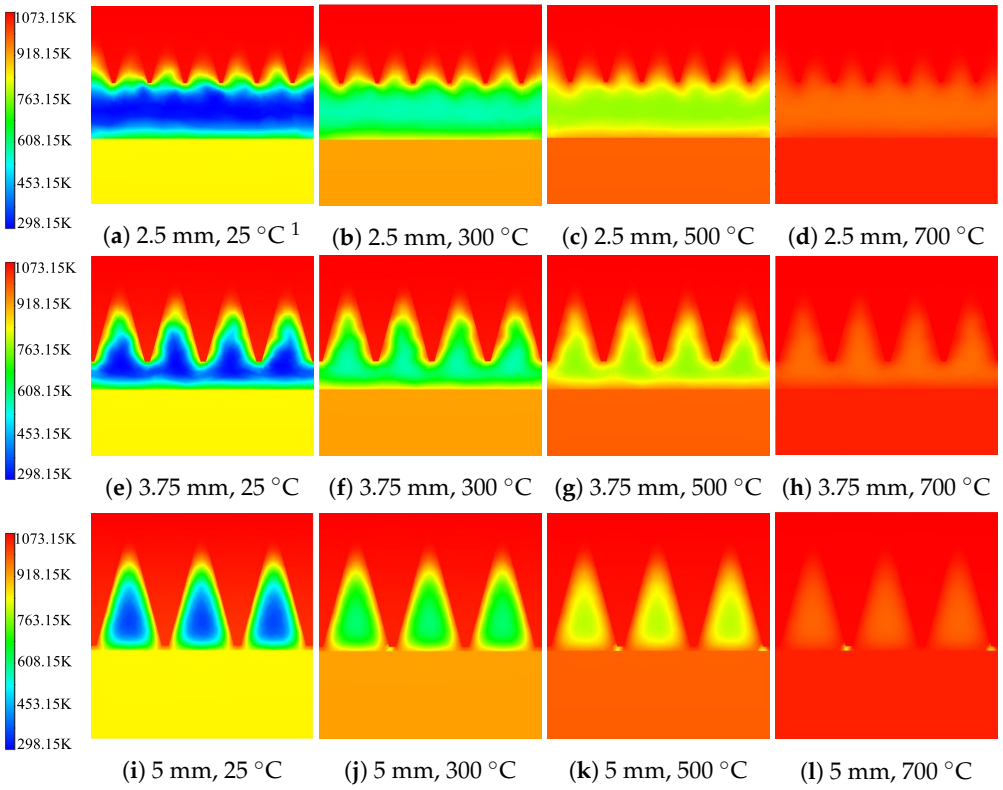


Figure 10. Outlet temperature distributions for fin apex angle of 30°. [1] Fin height and inlet temperature. Mass flow rate = 0.001 kg/s.

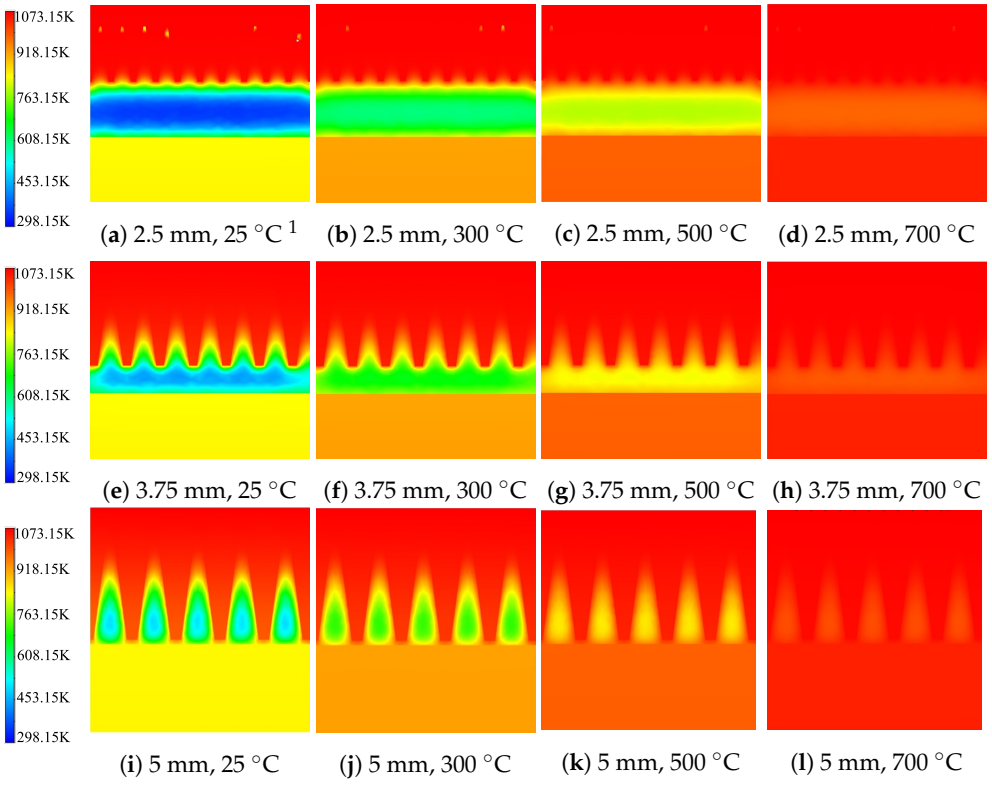


Figure 11. Outlet temperature distributions for fin apex angle of 15°. [1] Fin height and inlet temperature. Mass flow rate = 0.001 kg/s.

5.2. Pressure Drop

Pressure drop affects the heat transfer characteristics of the working fluid by changing its density and velocity. This makes pressure drop an important parameter in the design of the novel cavity receiver absorber.

5.2.1. Effect of Fin Dimensions in Different Heating Stages

Figure 12 demonstrates the relationship between pressure drop and incoming fluid temperature in the channel at a length of 100 mm that is subjected to an 800 °C heat source and 10 bar air pressure. The figure provides the comparative results for fins with different dimensions, e.g., fin heights ranging from 2.5 mm to 5 mm and apex angles of 15º and 30º.

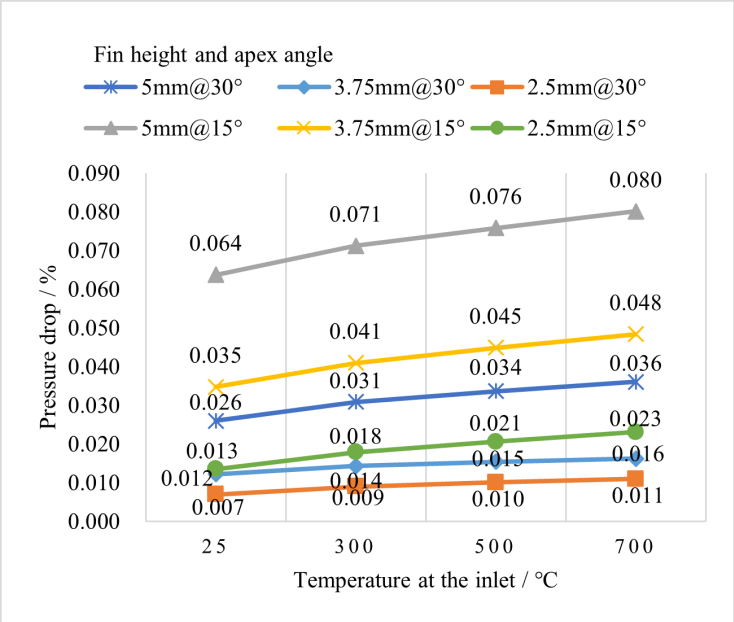


Figure 12. Pressure drop/% at different initial air temperatures. Inlet air flow at 10 bar, 0.001 kg/s, subject to 800 °C heat source per 100 mm of channel.

According to Figure 12, an increase in the inlet working fluid temperature results in an increased pressure drop percentage. For the novel WEDM processed finned channel with 5 mm fin height and an apex angle of 15°, the pressure drop changes from 0.064% to 0.080%. This phenomenon can be attributed to the fact that the heating of the working fluid within the finned channels leads to a decrease in its density, resulting in a higher volume flow rate. Consequently, the pressure drop caused by friction is amplified.

Figure 12 illustrates that when the fin height and air flow parameters are constant, a reduction in pressure drop is observed in channels featuring 30° fins compared to those with 15° fins. Specifically, for channels with 5 mm fins and an incoming flow at 25 °C, the pressure drop values for the two channels are 0.026% and 0.064%, respectively.

5.2.2. Effect of Pressure and Mass Flow Rates

Figure 13 depicts the relationship between the pressure drop and inlet fluid pressure in the channel at a length of 100 mm subjected to an 800 °C heat source and 5, 10, and 15 bar of air pressure.

According to Figure 13, an increase in inlet air pressure results in a decrease in pressure drop. Specifically, for a mass flow rate of 0.001 kg/s, an increase in the inlet air pressure from 5 bar to 15 bar causes a sharp reduction in the pressure drop percentage, from 0.233% to 0.029%; furthermore, this decrease in the pressure drop percentage is more significant with higher mass flow rates, with the pressure drop for air flow being 0.0015 kg/s > 0.001 kg/s > 0.0005 kg/s. At an inlet air temperature of 10 bar, the pressure

drop for a mass flow rate of 0.0015 kg/s is 0.108%, while the pressure drop for 0.0005 kg/s is 0.026%.

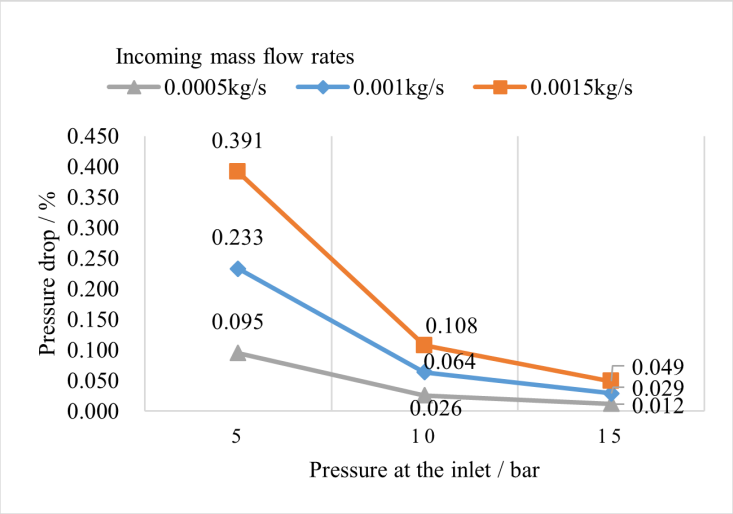


Figure 13. Pressure drop/% under different initial air pressures, subject to 800 °C heat source per 100 mm of channel.

5.2.3. Summary of Pressure Drop Results

Although the factors studied previously have a clear impact on pressure drop, it is observed that the percentage of pressure drop per 100 mm remains negligible in all cases, never exceeding 0.391% (at 5 bar) within the parameter range of this study and falling quickly with the increase in initial pressure. This indicates that the integration of WEDM-processed fins in the absorber does not increase the required pumping power. Consequently, the prospect of utilizing finned heat exchangers as a replacement for conventional tubular heat exchangers appears promising when compared to the outcomes reported in the literature [26].

5.3. Heat Transfer

Heat transfer is the key parameter that illustrates the thermal performance of the novel cavity receiver absorber.

5.3.1. Effect of Fin Dimensions in Different Heating Stages

Figure 14 demonstrates the relationship between heat transfer rate and incoming fluid temperature in the channel in the 100 mm of channel, subjected to an 800 °C heat source and 10 bar air pressure. The figure provides the comparative results for fins with different dimensions, e.g., fin heights ranging from 2.5 mm to 5 mm and varying apex angles of 15° and 30°.

Figure 14 reveals that an increase in initial temperature results in a decrease in heat transfer capability within the finned channel. Specifically, when a working fluid of 10 bar and 0.001 kg/s flow rate is used in a channel with a 5 mm fin height and 15° apex angle, the maximum heat transfer rate decreases from 376.4 W at an initial temperature of 25 °C to 52.26 W at an initial temperature of 700 °C. This trend suggests that as the working fluid is heated along the finned channel, the heat transfer rate with respect to the air flow gradually decreases.

Additionally, Figure 14 demonstrates that finned channels with a 15° apex angle achieve a higher heat transfer rate than those with a 30° apex angle when the fin heights are identical. Specifically, when an air flow with an initial temperature of 25 °C is heated in channels with 5 mm fins, the heat transfer rate in fins with a 15° apex angle is 376.4 W, whereas is 230.96 W in fins with a 30° apex angle.

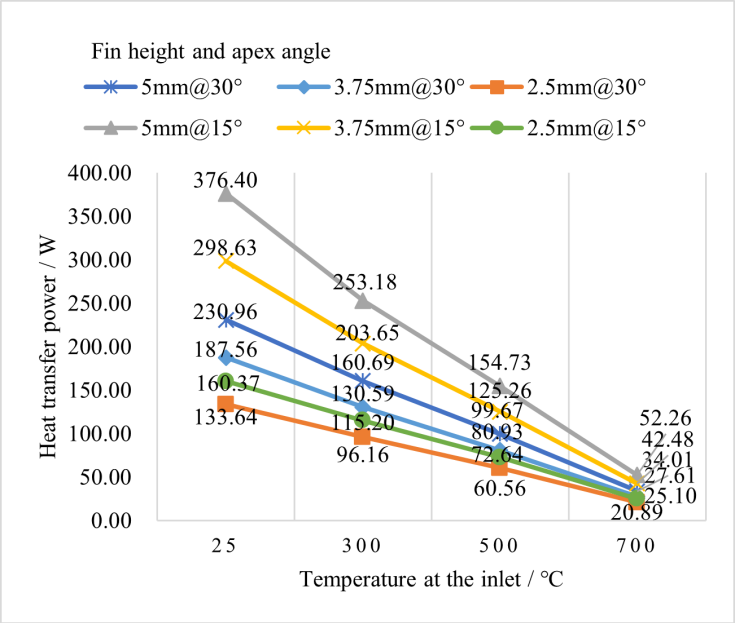


Figure 14. Heat transfer/W at different initial air temperatures. Inlet air at 10 bar, subject to 800 °C heat source per 100 mm of channel.

5.3.2. Effect of Mass Flow Rates

Table 2 presents the CFD heat flux outcomes obtained when air flow with an inlet temperature of 25 °C is exposed to a heat source of 800 °C. The enthalpy of the air undergoes negligible modifications of less than 0.1% over a temperature range from 25 °C to 800 °C and a pressure range from 5 bar to 15 bar. Thus, the impact of the novel design's pressure parameter on heat transfer can be disregarded in the present study.

Table 2. Heat transfer for different mass flow rates [1].

Mass Flow Rate/kg·s^{-1}	0.0005	0.001	0.0015
Heat flux/W	239.6	376.0	482.7
Final temperature/°C	502.97	400.24	346.31

[1] For the designated mass flow rate, the pressure is 5 bar, 10 bar, and 15 bar, respectively, and the initial temperature is 25 °C.

The findings in Table 2 suggest that alterations in mass flow rate from 0.0005 kg/s to 0.0015 kg/s exert a substantial influence on the heat transfer rate. Specifically, the maximum heat transfer rate per 100 mm of channel is augmented from 239.6 W to 482.7 W, or 101.5%, at an initial temperature of 25 °C.

5.3.3. Summary of Numerical Results of Heat Transfer

Based on the numerical findings, it is recommended that the fin height be in close proximity to the total channel height (5 mm in this paper). With regard to the apex angle, a smaller angle is advantageous in terms of heat transfer due to reduced thermal resistance, and is to be preferred in all designs. However, it should be noted that the heat transfer rate may surpass the heat source's power at temperatures exceeding 300 °C owing to significant heat loss through radiation and convection [24]. Alternatively, opting for larger apex angles that facilitate manufacturing may be a feasible option.

5.4. Static Structural Results

The stiffness and strength of an absorber featuring finned channels with 15° apex angles and height of 5 mm were evaluated using the setup outlined in Appendix C. Under a working pressure of 10 MPa, the maximum strain and stress were found to be

0.00036 mm/mm and 72 MPa, respectively. These results indicate that the design with a 5 mm fin height and 15° apex angle provides a sufficient safety margin for further experimental investigation. Preliminarily, we believe that this new design structure meets the requirements of state-of-the-art CSP systems, particularly those with relatively low working pressures.

5.5. Experimental Results

The experiment results represent the maximum heat transfer capability of the novel absorber under the specific experimental conditions when not surpassing the flat panel heater's available heating power. The heater's nominal heating power before reaching the target temperature is 2000 W; however, after deducting the heat loss of the absorber, determined using the method in [24], the available heating power turns out to be around 1455 W at 400 °C. The thermal power transferred to the working fluid should not exceed this value when heated at 400 °C. The values measured in the experiment are listed in Table 3.

Table 3. Comparison of experimental and numerical results.

	Experimental	**Numerical**
Temperature (heat source)/°C	400	400
Temperature (inlet)/°C	21.7	21.7
Temperature (outlet)/°C	346.5	358.484
Pressure (inlet, gauge)/Pa	8.00×10^5	8.01×10^5
Pressure (outlet, gauge)/Pa	7.99×10^5	8.00×10^5
Massflow rate/kg/h	12	12
Heat transfer/W	1113.033 (96.6741%)	1151.326 (100%)

The working fluid in the experiment was compressed air.

The enthalpy values for air at 8.00 bar (gauge), 21.7 °C and 7.99 bar (gauge), 346.5 °C are 293.26 kJ/kg and 628.17 kJ/kg, respectively. The heat transfer to the compressed air in the experiment is listed in Table 3. By expanding the length of the channel in Section 2.2 to 160 mm and revising the boundary conditions according to the experimental results, the outlet temperature and heat transfer rate obtained in the calculation domain are listed in Table 3.

Uncertainties

Uncertainties and their impacts on the gauges, including the flow meter, thermocouples, and pressure gauges, are listed in Table 4.

Table 4. Gauge value uncertainties and their impact on heat transfer.

Gauge	**Uncertainty**	**Impact on Heat Transfer**
Flow meter	±1%	±1% [1]
Thermocouple (inlet)	±0.5%	– [2]
Thermocouple (outlet)	±1%	– [2]
Thermocouple (heater)	±2.5 °C	±0.39% [1]
Pressure gauge (inlet)	±1%	– [2]
Pressure gauge (outlet)	±1%	– [2]

[1] Values with a direct impact on heat transfer. [2] Values with an indirect impact on heat transfer which need to be considered along with other uncertainty values.

The impact of heat transfer caused by the temperature and pressure gauge uncertainties listed in Table 4 are around ±1.13% under the conditions listed in Table 3. Thus, the uncertainty of the experimental heat transfer results at the minimum limit is

$$(1 - 1\%) \times (1 - 0.39\%) \times (1 - 1.13\%) - 1 = -2.5\%. \quad (2)$$

Additionally, the uncertainty of the experimental heat transfer results at the maximum limit is

$$(1 + 1\%) \times (1 + 0.39\%) \times (1 + 1.13\%) - 1 = 2.7\%. \quad (3)$$

Based on the results of the uncertainty analysis, it can be concluded that the experimental results in this study are subject to a certain degree of uncertainty of about −2.5% under the tested experimental conditions. Compared with the outcome error of −3.33%, the following issues may explain the extra error in the experimental results:

- An additional error might exist when combining the numerical results acquired in 10 mm wide domains. Adjacent boundaries are set as adiabatic walls (flux = 0) when calculated separately, and these boundaries do not actually exist.
- After reaching the designated heating temperature at constant 400 °C, there is a time interval before the heater resumes heating after detecting a temperature drop. The temperature drop in this interval may reach 2.5 °C.
- The high temperature thermocouple was installed about 100 mm away from the exit of the absorber, which may have affected the measured temperature value even with proper insulation.
- Before and after the pressurized air is heated in the finned channels, it passes through two smooth channels in the absorber with 7 mm × 10 mm sections, respectively. These two smooth channels could have an effect on the fluid temperature.

Despite these possibilities, our experimental investigations validate the numerical results with a relatively small margin of error.

5.6. Comparison with Previous Research

5.6.1. CFD Results

The concept in this research is novel, and differs from previous research in its geometry, dimensions, working fluid type, pressure and temperature either thoroughly or partially; thus, a comparison of CFD results was carried out, as illustrated in Figure 15.

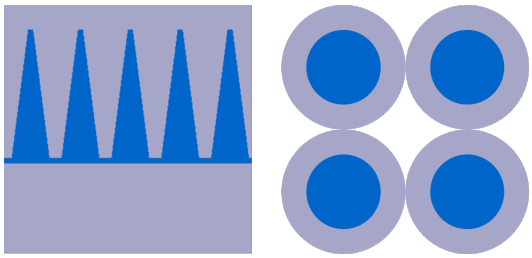


Figure 15. Comparison with heat transfer via tubes (CFD models).

Air flows with an initial temperature of 25 °C and 10 bar pressure were injected into four 100 mm steel tubes with an internal diameter of 3 mm and external diameter of 5 mm. The flow rate was 0.001 kg/s (0.00025 kg/s per tube). This results in a maximum heat transfer rate of approximately 173 W in total. In contrast, the tested finned channels with 3.75 mm or 5 mm fin height and 15° generated a maximum heat transfer rate 72.6% and 117.6% higher in the calculation domain than tubes occupying an equivalent volume. The heat transfer rate in the novel finned channels was superior to that observed in traditional tubular absorbers with equivalent length and volume.

5.6.2. Experimental Results

Results obtained in previous research are listed in Table 5.

Table 5. Heat transfer comparison with previous research.

	This Research	Research 1 [27]	Research 2 [28]	Research 3 [29]
Working fluid	Air	Air	Nitrogen	Air
Pressure/bar	8	5–7.5	< 6.5	6.9
Heating temperature/°C	400	300–500	205	100–400
Heater volume/mm^3	$\sim 361,000$ [1]	$\sim 769,690$ [2]	$\sim 303,327$ [3]	$\sim 331,490$ [4]
Heat transfer/W	1113	< 1218 [5]	231	< 600

[1] The external volume of the absorber. [2] The internal volume of the tubes; the space between the tubes could not be calculated. [3] The external volume of the tubes; the space between the tubes could not be calculated. [4] Sweep volume + dead volume; the external volume could not be calculated. [5] Power of the Stirling engine; the heat transfer in the heater may surpass twice this value.

The novel design has comparable if not superior heat transfer capability, and has the potential to be further improved for application in CSP systems.

6. Conclusions

This paper proposes a novel non-tubular cavity receiver absorber with extended surfaces (fins) to enhance heat transfer. A simplified model was developed to numerically investigate the effects of the dimensional factors of the fins and the thermohydraulic parameters of the working fluid on the pressure drop reduction and heat transfer enhancement in the absorber's finned channels. In addition, the heat transfer in the prototype absorber, which was manufactured by welding two parts with WEDM-processed extended surfaces, was investigated experimentally. The following conclusions can be drawn from this study:

1. The implementation of extended surfaces in cavity receiver absorbers can significantly improve heat transfer by reducing thermal resistance in the solid material, expanding the fluid–solid interface, and decreasing the distance between the flow center and the interface. In comparison to conventional tubular absorbers without fins, the novel absorber proposed in this paper demonstrates superior heat transfer performance and temperature distribution at the exit when the structures occupy comparable volumes.
2. As the heating temperature increases beyond a certain point, the heat transfer to the working fluid decreases due to a significant increase in heat loss. However, the novel absorber has a smaller external surface area and is more able to apply insulation compared to conventional tubular absorbers, resulting in lower heat loss. This means that the heat transfer degradation with rising temperature is slower when occupying the same volume.
3. At the typical working pressure of 10 bar, the pressure drop caused by friction in the fin surfaces along the working flow direction does not exceed 0.06% per 100 mm in the designs studied in this research, and this percentage decreases with increasing pressure. This suggests that the novel absorber's length could be customized to meet the demands of state-of-the-art CSP applications.
4. In addition to their heat transfer function, the extended surfaces in the novel absorber act as stiffeners, improving the compressive strength of the heat transfer plane. The compressive strength of the absorber experimentally tested in this study (160 mm $\times$ 160 mm) is capable of withstanding pressures comparable to those present in conventional tubular absorbers.

This research includes the following limitations:

- Meshing of multi-scale structures generates an excessive number of elements, which may have exceeded 100 million in the studied case. The adapted calculation domains are only representative subsets of the entire absorber structure.
- The flat panel heaters' heating power generation was limited, and was unable to reach the maximum heat transfer rate acquired in numerical investigations at higher temper-

atures. In order to fully compare the numerical and experiment results, an additional CFD investigation with lower performance must be performed.
- The absorber in the novel modular collector has not yet been tested under real solar radiation.
- The intended use of the absorber is for either a novel CSP system, such as the one mentioned in [24], or a traditional tower system. The present research only considered the former case, as the geometric dimensions of the scheme were more suitable for laboratory experiments. However, the latter case is more practical for rel-world application.

In the future, more research is needed in several areas to realize the application of the proposed novel absorber:

- The absorber should be installed in a CSP testing system under real solar rediation;
- The channel height, fin height, and fin width should be optimized, especially for systems operating at higher temperatures;
- The fin surfaces can be fabricated with specific microstructures or painted to enhance heat transfer;
- It is expected that the absorber will be redesigned and investigated for application in tower systems.

Author Contributions: Conceptualization, Y.Y. and X.N.; methodology, X.N.; validation, X.N.; formal analysis, X.N.; investigation, X.N.; resources, Y.Y. and J.D.; data curation, X.N.; writing—original draft preparation, X.N.; writing—review and editing, Y.Y.; supervision, Y.Y. and J.D.; project administration, Y.Y.; funding acquisition, Y.Y. and J.D. All authors have read and agreed to the published version of the manuscript.

Funding: This research was funded by National Natural Science Foundation of China grant number CA24401070.

Conflicts of Interest: The authors declare no conflict of interest. The funders had no role in the design of the study, in the collection, analysis, or interpretation of data, in the writing of the manuscript, or in the decision to publish the results.

Abbreviations

The following abbreviations are used in this manuscript:

AA	Apex Angle
CSP	Concentrated Solar Power
CFD	Computational Fluid Dynamics
FEM	Finite Element Method
FH	Fin Height
FW	Fin Width
WEDM	Wire Electrical Discharge Machining

Appendix A. Governing Equations in ANSYS Fluent

The governing equations integrated in the ANSYS software can be found on the corresponding pages in the technical file *Ansys Fluent Theory Guide 2022* (the Guide). The continuity equation on page 3 in the Guide for flow in a non-accelerating reference frame is

$$\partial P/\partial t + \nabla \cdot (\rho \overrightarrow{v}) = S_m \tag{A1}$$

The momentum equation on page 3 in the Guide in this case is

$$\partial(\rho \overrightarrow{v})/\partial t + \nabla \cdot (\rho \overrightarrow{v} \overrightarrow{v}) = -\nabla p + \nabla \cdot (\bar{\bar{\tau}}) + \rho \overrightarrow{g} + \overrightarrow{F} \tag{A2}$$

Ansys Fluent solves the energy equation on page 160 in the Guide in the following form:

$$\partial(\rho(e+v^2/2))/\partial t + \nabla\cdot(\rho v(h+v^2/2)) = \nabla\cdot(k_{eff}\nabla T - \sum_j h_j \overrightarrow{J_j} + \bar{\bar{\tau}}_{eff}\cdot\overrightarrow{v}) + S_h \quad \text{(A3)}$$

Appendix B. Additional CFD Investigations

Appendix B.1. Fluid Flow Characteristics

Fluid flow characteristics in channels are investigated using a model which includes the fluid body. Pressurized air enters the domain from a mass flow inlet boundary, flows through the finned channels, and exits through a pressure outlet domain. The fluid flow is expected to encounter moment change before and after passing through the finned channels. Thus, the two parts of the smooth channels before and after the finned channels are connected to the finned channels, as illustrated in Figure A1.

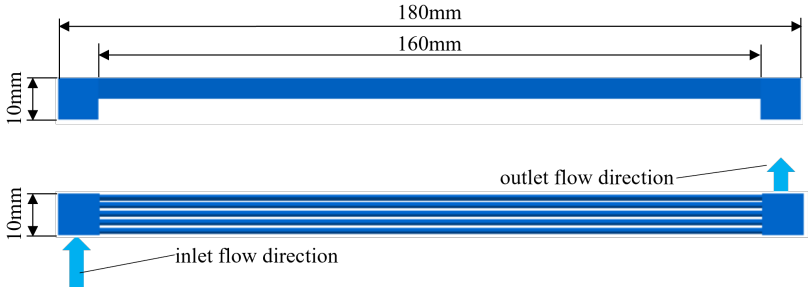


Figure A1. Numerical model for fluid characteristics.

The CFD investigation shares the continuity and momentum governing equations in Section 3 and Appendix A, while the energy equation is not adapted in this calculation. Except for the mass flow inlet and pressure outlet boundaries, the other boundaries are defined as walls. The mass flow inlet boundary is 1 MPa at the flow rate of 0.001 kg/s, the fin heights are 5 mm, and the apex angles are 15°. The meshing setups are identical to those adapted in Section 3.3. These different setups are briefly summarized below:

- Modeling: no solid body, additional channel added
- Governing equations: no energy equation
- Boundary conditions: same inlet and outlet, no heat transfer on walls
- Numerical method: same
- Grid generation: same.

Appendix B.2. Temperature Distribution in the Channel

The temperature distribution in the channel is investigated numerically, similarly to Section 2.2. The 100 mm length of the calculation domain in Section 2.2 along the flow direction is extended to 160 mm. The model is briefly presented in Figure A2.

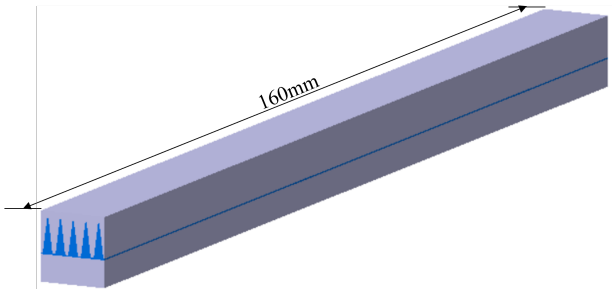


Figure A2. Extended numerical model for temperature distribution.

The governing equations, boundary conditions, numerical methods, and meshing are all identical to those applied in Section 3 and Appendix A. The fin heights are 5 mm and the apex angles are 15°. These different setups are briefly summarized below:

- Modeling: length extended to 160 mm
- Governing equations: same
- Boundary conditions: same
- Numerical method: same
- Grid generation: same.

Appendix C. The Heat Transfer Plate's Static Structural Properties

The strength and stiffness of the heat transfer plate where the fins are fabricated are validated through a basic static structural FEM analysis. The numerical model is illustrated in Figure A3. The model includes the independent part of the heat transfer plate without welding to the bottom plate.

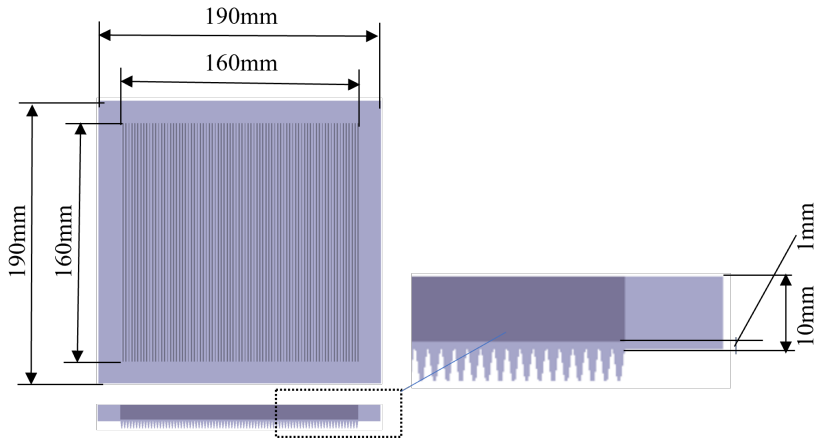


Figure A3. Numerical model for static structural analysis.

The fin heights are 5 mm and the apex angles are 15°. The meshing sizes on top of the fins are 0.2 mm, and all other elements are 0.8 mm. The meshed model has about 3,727,778 elements, with an average meshing quality of 0.715. The meshing results are illustrated in Figure A4.

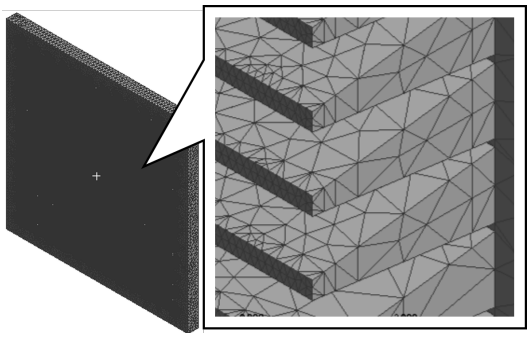


Figure A4. Meshing detail of the static structural model.

To execute the validation of strength, the fixed support is applied on all four side surfaces of the model. A static pressure of 10 MPa is loaded on the fins and the finned surface. The load and support are demonstrated in Figure A5.

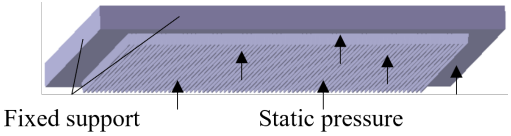


Figure A5. Loads and support applied in the static structural model.

References

1. Zhou, Y. Worldwide Carbon Neutrality transition? Energy efficiency, renewable, Carbon Trading and Advanced Energy Policies. *Energy Rev.* **2023**, *2*, 100026. [CrossRef]
2. Poživil, P.; Aga, V.; Zagorskiy, A.; Steinfeld, A. A Pressurized Air Receiver for Solar-driven Gas Turbines. *Energy Procedia* **2014**, *49*, 498–503. [CrossRef]
3. Mousavi Ajarostaghi, S.S.; Zaboli, M.; Javadi, H.; Badenes, B.; Urchueguia, J.F. A Review of Recent Passive Heat Transfer Enhancement Methods. *Energies* **2022**, *15*, 986. [CrossRef]
4. Nada, S.; Said, M. Effects of Fins geometries, arrangements, Dimensions and Numbers on Natural Convection Heat Transfer Characteristics in finned-horizontal Annulus. *Int. J. Therm. Sci.* **2019**, *137*, 121–137. [CrossRef]
5. Ammar Ali, M.; Sajid, M.; Uddin, E.; Bahadur, N.; Ali, Z. Numerical Analysis of Heat Transfer and Pressure Drop in Helically Micro-Finned Tubes. *Processes* **2021**, *9*, 754. [CrossRef]
6. Lin, Y.; Li, J.; Chen, Z.; Li, W.; Ke, Z.; Ke, H. Two-Phase Flow Heat Transfer in Micro-Fin Tubes. *Heat Transf. Eng.* **2019**, *42*, 369–386. [CrossRef]
7. Wei, L. Study on Comprehensive Performance Evaluation for Condensation Heat Transfer inside the micro-fin Tube. *Adv. Mech. Eng.* **2020**, *12*, 168781402094009. [CrossRef]
8. Tang, W.; Li, W.; Minkowycz, W.J. A Numerical Investigation of Convective Condensation in micro-fin Tubes of Different Geometries. *Numer. Heat Transf. Part Appl.* **2020**, *78*, 697–705. [CrossRef]
9. Zhang, J.N.; Cheng, M.; Ding, Y.D.; Fu, Q.; Chen, Z.Y. Influence of Geometric Parameters on the gas-side Heat Transfer and Pressure Drop Characteristics of three-dimensional Finned Tube. *Int. J. Heat Mass Transf.* **2019**, *133*, 192–202. [CrossRef]
10. Duan, L.; Ling, X.; Peng, H. Flow and Heat Transfer Characteristics of a double-tube Structure Internal Finned Tube with Blossom Shape Internal Fins. *Appl. Therm. Eng.* **2018**, *128*, 1102–1115. [CrossRef]
11. Kim, T.; Choi, B.I.; Han, Y.S.; Do, K.H. Experimental and Analytical Investigation of a Wavy Fin Recuperator for a Micro Gas Turbine. *Int. J. Heat Mass Transf.* **2020**, *148*, 118998. [CrossRef]
12. Lotfi, B.; Zeng, M.; Sundén, B.; Wang, Q. 3D Numerical Investigation of Flow and Heat Transfer Characteristics in Smooth Wavy fin-and-elliptical Tube Heat Exchangers Using New Type Vortex Generators. *Energy* **2014**, *73*, 233–257. [CrossRef]
13. Zhou, Y. Demand Response Flexibility with Synergies on Passive PCM walls, BIPVs, and Active air-conditioning System in a Subtropical Climate. *Renew. Energy* **2022**, *199*, 204–225. [CrossRef]
14. Zheng, X.; Zhou, Y. A three-dimensional Unsteady Numerical Model on a Novel aerogel-based PV/T-PCM System with Dynamic heat-transfer Mechanism and Solar Energy Harvesting Analysis. *Appl. Energy* **2023**, *338*, 120899. [CrossRef]
15. Dastmalchi, M.; Sheikhzadeh, G.; Arefmanesh, A. Optimization of micro-finned Tubes in Double Pipe Heat Exchangers Using Particle Swarm Algorithm. *Appl. Therm. Eng.* **2017**, *119*, 1–9. [CrossRef]
16. Freegah, B.; Hussain, A.A.; Falih, A.H.; Towsyfyan, H. CFD Analysis of Heat Transfer Enhancement in plate-fin Heat Sinks with Fillet profile: Investigation of New Designs. *Therm. Sci. Eng. Prog.* **2020**, *17*, 100458. [CrossRef]
17. Hussain, A.A.; Freegah, B.; Khalaf, B.S.; Towsyfyan, H. Numerical Investigation of Heat Transfer Enhancement in Plate-Fin Heat sinks: Effect of Flow Direction and Fillet Profile. *Case Stud. Therm. Eng.* **2019**, *13*, 100388. [CrossRef]
18. Sahel, D.; Bellahcene, L.; Yousfi, A.; Subasi, A. Numerical Investigation and Optimization of a Heat Sink Having Hemispherical Pin Fins. *Int. Commun. Heat Mass Transf.* **2021**, *122*, 105133. [CrossRef]
19. Yan, Y.; Zhao, T.; He, Z.; Yang, Z.; Zhang, L. Numerical Investigation on the Characteristics of Flow and Heat Transfer Enhancement by Micro pin-fin Array Heat Sink with fin-shaped Strips. *Chem. Eng. Process. Process Intensif.* **2021**, *160*, 108273. [CrossRef]
20. Singh, P.; Patil, A.K. Experimental Investigation of Heat Transfer Enhancement through Embossed Fin Heat Sink under Natural Convection. *Exp. Therm. Fluid Sci.* **2015**, *61*, 24–33. [CrossRef]
21. Özbektas, S.; Sungur, B.; Topaloglu, B. Numerical Investigation of the Effect of Heat Sinks with Various Fin Geometries on the Performance of a Thermoelectric Generator. *J. Therm. Sci. Eng. Appl.* **2022**, *15*, 031004. [CrossRef]
22. Xu, R.; Wang, G.; Jiang, P. Spray Cooling on Enhanced Surfaces: A Review of the Progress and Mechanisms. *J. Electron. Packag.* **2021**, *144*, 010802. [CrossRef]
23. Pai, Y.W.; Yeh, R.H. Experimental Investigation of Heat Transfer and Pressure Drop Characteristics of Internal Finned Tubes. *Int. J. Heat Mass Transf.* **2022**, *183*, 122183. [CrossRef]
24. Na, X.; Yao, Y.; Zhao, C.; Du, J. Heat Loss Reduction Approach in Cavity Receiver Design Based on Performance Investigation of a Novel Positive Conical Scheme. *Energies* **2022**, *15*, 784. [CrossRef]
25. Li, Y.; Xia, G.; Ma, D.; Jia, Y.; Wang, J. Characteristics of Laminar Flow and Heat Transfer in Microchannel Heat Sink with Triangular Cavities and Rectangular Ribs. *Int. J. Heat Mass Transf.* **2016**, *98*, 17–28. [CrossRef]
26. Lei, Y.; Li, Y.; Jing, S.; Song, C.; Lyu, Y.; Wang, F. Design and Performance Analysis of the Novel shell-and-tube Heat Exchangers with Louver Baffles. *Appl. Therm. Eng.* **2017**, *125*, 870–879. [CrossRef]
27. Gheith, R.; Hachem, H.; Aloui, F.; Nasrallah, S.B. Experimental and Theoretical Investigation of Stirling Engine heater: Parametrical Optimization. *Energy Convers. Manag.* **2015**, *105*, 285–293. [CrossRef]

28. Xiao, G.; Chen, C.; Shi, B.; Cen, K.; Ni, M. Experimental Study on Heat Transfer of Oscillating Flow of a Tubular Stirling Engine Heater. *Int. J. Heat Mass Transf.* **2014**, *71*, 1–7. [CrossRef]
29. García, D.; Prieto, J. A non-tubular Stirling Engine Heater for a Micro Solar Power Unit. *Renew. Energy* **2012**, *46*, 127–136. [CrossRef]

Disclaimer/Publisher's Note: The statements, opinions and data contained in all publications are solely those of the individual author(s) and contributor(s) and not of MDPI and/or the editor(s). MDPI and/or the editor(s) disclaim responsibility for any injury to people or property resulting from any ideas, methods, instructions or products referred to in the content.